Nucleation and growth kinetics for intercalated islands during deposition on layered materials with isolated pointlike surface defects

Yong Han,[1,2] A. Lii-Rosales,[1,3] Y. Zhou,[1,4] C.-J. Wang,[5] M. Kim,[1,2] M. C. Tringides,[1,2] C.-Z. Wang,[1,2] P. A. Thiel,[1,3,6] and James W. Evans[1,2,7]

[1]*Ames Laboratory–USDOE, Iowa State University, Ames, Iowa 50011, USA*
[2]*Department of Physics and Astronomy, Iowa State University, Ames, Iowa 50011, USA*
[3]*Department of Chemistry, Iowa State University, Ames, Iowa 50011, USA*
[4]*Department of Physics, Xiamen University, Xiamen 361005, China*
[5]*Department of Mathematics, National Chung Cheng University, Chiayi 62102, Taiwan*
[6]*Department of Materials Science and Engineering, Iowa State University, Ames, Iowa 50011, USA*
[7]*Department of Mathematics, Iowa State University, Ames, Iowa 50011, USA*

(Received 8 June 2017; revised manuscript received 14 August 2017; published 13 October 2017)

Theory and stochastic lattice-gas modeling is developed for the formation of intercalated metal islands in the gallery between the top layer and the underlying layer at the surface of layered materials. Our model for this process involves deposition of atoms, some fraction of which then enter the gallery through well-separated pointlike defects in the top layer. Subsequently, these atoms diffuse within the subsurface gallery leading to nucleation and growth of intercalated islands nearby the defect point source. For the case of a single point defect, continuum diffusion equation analysis provides insight into the nucleation kinetics. However, complementary tailored lattice-gas modeling produces a more comprehensive and quantitative characterization. We analyze the large spread in nucleation times and positions relative to the defect for the first nucleated island. We also consider the formation of subsequent islands and the evolution of island growth shapes. The shapes reflect in part our natural adoption of a hexagonal close-packed island structure. Motivation and support for the model is provided by scanning tunneling microscopy observations of the formation of intercalated metal islands in highly-ordered pyrolytic graphite at higher temperatures.

DOI: 10.1103/PhysRevMaterials.1.053403

I. INTRODUCTION

There have been extensive studies of the homogeneous nucleation and growth of metal islands, also described as nanoclusters, during surface deposition on wide defect-free terraces [1–3]. Here, deposition provides a uniform flux of atoms onto the surface leading to an initial uniform buildup in the density of diffusing adatoms. This in turn leads to nucleation of islands initially at random locations and subsequent competition between nucleation of new islands and growth of existing islands. Such subsequent nucleation is persistent and tends to occur away from existing islands where the quasi-steady-state adatom density has local maxima [3].

For nucleation and growth of intercalated metal islands in the gallery between the top two layers of periodically-layered materials such as highly oriented pyrolytic graphite (HOPG), one anticipates a quite different picture. We focus on one scenario where some fraction of atoms deposited on the surface can access the gallery just under the top layer of the substrate through well-separated pointlike defects in the top layer. This fraction will be controlled by the density of traps for diffusing adatoms on the top surface (i.e., by any surface adsorbate islands and by step edges), by the presence of any additional barrier to access the subsurface gallery, and generally also by thermodynamic factors. The intercalated adatom density will build up inhomogeneously around each defect "point source." Eventually, an island will nucleate, generally at some distance from the defect, and subsequent island growth will occur. Such growth could be preferentially biased back toward the point-source defect (see Fig. 1). Once that island grows back to the defect, it may block injection of further atoms at that defect, and in fact may seed growth of a surface adsorbate island on top of the defect (see Sec. V for examples). In general, nucleation of additional islands will also occur preferentially at locations away from existing islands. Motivation for the above scenario comes from recent experimental studies of the deposition at around 800 K of various metals, including Cs [4], Dy, Ru, and Cu [5], on a defective HOPG surface. In these studies, HOPG was sputtered by Ar^+ ions to produce damage in the form of local or pointlike surface defects.

A few additional observations are also appropriate as background for our analysis. First, amongst the above-mentioned experimental studies, we note that for near-surface Cs intercalation on HOPG [6], vacancy cluster defects in the top HOPG layer were explicitly identified as the entry points for Cs intercalation. However, it was also shown that the defects must consist of more than four missing C atoms in order for intercalation to be energetically viable. Second, in addition to the above experimental studies, and also the current theoretical analysis focused on the formation of near-surface intercalated islands, we emphasize that there exists a substantial literature on the overall intercalation process leading to formation of bulk graphite intercalation compounds (GICs). In particular, these studies consider kinetics for the multiple aspects and stages of the formation of GICs [6–8]. Third, beyond intercalation studies, there are also numerous previous investigations of the formation of surface islands, and the decoration of step edges, by deposition of various metals including Dy [9] on HOPG [10].

The outline of subsequent sections of this paper is as follows. Section II presents an analytic treatment of various

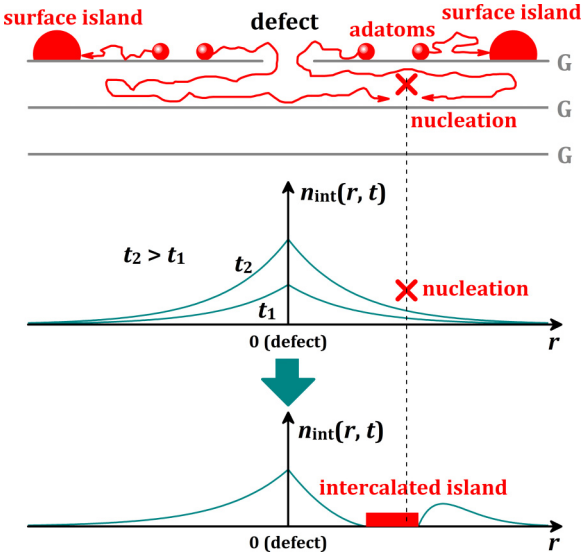

FIG. 1. Schematic of model for nucleation and growth of intercalated islands. G denotes an individual layer in substrate, e.g., a graphene layer in HOPG. Intercalated adatom density $n_{\rm int}(r,t)$ is a function of time t and the distance r from the defect at $r = 0$.

aspects of the above point-source-mediated nucleation process. Most emphasis is on a continuum deposition-diffusion equation treatment for nucleation of the first island. Then, in Sec. III, we develop a suitably crafted stochastic atomistic-level lattice-gas model for single-layer intercalated islands which can elucidate both the nucleation process as well as subsequent island growth shapes. Results for this model obtained from kinetic Monte Carlo (KMC) simulations are presented in Sec. IV. Finally, Sec. V provides further discussion of the modeling including application to analysis of metal-HOPG systems.

II. CONTINUUM TREATMENT FOR NUCLEATION OF INTERCALATED ISLANDS

As a preliminary analysis, we estimate the rate, $J_{\rm int}$, at which atoms intercalate at each isolated pointlike defect for typical deposition experiments on defective graphite. Based on the above-mentioned study of intercalation of Cs [4], and our own analysis for Dy, we anticipate the existence of a substantial additional barrier Δ (above the terrace diffusion barrier) which must be surmounted to inject adatoms through the defect into the gallery. Then, one can regard the density of deposited adatoms on the top surface, $n_{\rm ad}$, as being in a steady state corresponding to a rough balance between gain due to deposition at rate F and loss due to aggregation with traps on the surface. If the latter are assumed to be primarily surface islands with density $N_{\rm isl}$, then one has that $F \approx \sigma_{\rm isl} D_{\rm surf} N_{\rm isl} n_{\rm ad}$ [1,3]. Here, $\sigma_{\rm isl} \sim 1$ is the capture number for these surface islands, and $D_{\rm surf}$ is the surface diffusion coefficient. Then, the injection rate is simply estimated from $J_{\rm int} \approx D_{\rm surf} n_{\rm ad} \exp(-\beta\Delta) \approx (F/N_{\rm isl}) \exp(-\beta\Delta)$. Here, $\beta \equiv 1/(k_{\rm B}T)$, where $k_{\rm B}$ denotes Boltzmann's constant and T the surface temperature. For experiments of metal intercalation on graphite, reasonable parameter values are $F \approx 0.05$ monolayers per second, $N_{\rm isl} \approx 10^{-4}$ per adsorption site, and $\Delta \approx 0.4$ to 0.6 eV. Then, at 800 K, one obtains $J_{\rm int} \approx 0.1$ to 1.5 atoms per second.

In the remainder of this section, we focus on analysis of the evolution of the density, $n_{\rm int} = n_{\rm int}(\boldsymbol{r},t)$, per unit area at position $\boldsymbol{r}$ and time t, of intercalated atoms fed by a single isolated point-source defect located at the origin $\boldsymbol{r} = 0$. We let $D_{\rm int}$ denote the diffusion rate for isolated intercalated atoms, and $J_{\rm int}$ denotes the total rate of injection of adatoms at the defect as above. Then, in the idealized case of a negligible defect radius, one must analyze the two-dimensional deposition-diffusion equation

$$\frac{\partial n_{\rm int}(\boldsymbol{r},t)}{\partial t} = D_{\rm int}\nabla^2_{\boldsymbol{r}} n_{\rm int}(\boldsymbol{r},t) + J_{\rm int}\delta(\boldsymbol{r}). \tag{1}$$

We now describe a more realistic alternative to incorporation of the singular delta-function source term, which accounts for a small but finite effective defect radius $r_{\rm d}$. One can instead analyze the above equation without the source term for $r_{\rm d} \leqslant r = |\boldsymbol{r}| < \infty$ after imposing the appropriate flux boundary condition, $-2\pi r D_{\rm int} \frac{\partial n_{\rm int}}{\partial r} = J_{\rm int}$, at $r = r_{\rm d}$ (corresponding to a total injection flux of $J_{\rm int}$). This latter approach is naturally adopted in numerical analysis. The natural rescaling of position, time, and density for either approach has the form

$$n_{\rm int}(\boldsymbol{r},t) = \frac{J_{\rm int}}{D_{\rm int}} C_{\rm int}(\tilde{\boldsymbol{r}},\tilde{t}), \quad \text{for } \tilde{\boldsymbol{r}} \equiv \boldsymbol{r}/(D_{\rm int}/J_{\rm int})^{1/2} \quad \text{and}$$
$$\tilde{t} \equiv J_{\rm int} t. \tag{2}$$

Here, $C_{\rm int}(\tilde{\boldsymbol{r}},\tilde{t})$ corresponds to a rescaled intercalated atom density. Then, it follows that this rescaled density satisfies

$$\frac{\partial C_{\rm int}(\tilde{\boldsymbol{r}},\tilde{t})}{\partial \tilde{t}} = \nabla^2_{\tilde{\boldsymbol{r}}} C_{\rm int}(\tilde{\boldsymbol{r}},\tilde{t}) + \delta(\tilde{\boldsymbol{r}}), \tag{3}$$

if one includes the two-dimensional (2D) delta-function source and uses the relation $\delta(\boldsymbol{r}/(D_{\rm int}/J_{\rm int})^{1/2}) = (D_{\rm int}/J_{\rm int})\delta(\boldsymbol{r})$. Alternatively, for the formulation with the flux boundary condition, one drops this source and imposes the condition $-2\pi\tilde{r}\frac{\partial C_{\rm int}}{\partial \tilde{r}} = 1$, at $\tilde{r} = |\tilde{\boldsymbol{r}}| = \tilde{r}_{\rm d} \equiv r_{\rm d}/(D_{\rm int}/J_{\rm int})^{1/2}$. From either formulation, it is clear that $C_{\rm int}(\tilde{\boldsymbol{r}},\tilde{t}) \approx -\frac{1}{2\pi}\ln(\tilde{r})$ for small $\tilde{r}$, with a weak dependence on t. In Sec. II A, we present an analytic treatment for the prenucleation regime where Eq. (3) is solved for an infinite spatial domain with initial condition $C_{\rm int}(\tilde{\boldsymbol{r}},t=0) = 0$, and where additional scaling behavior emerges. The results can be used to assess nucleation kinetics. In Sec. II B, we briefly discuss numerical analysis of this equation in the post-nucleation regime where intercalated islands have formed. In this regime, a nontrivial boundary value problem must be considered as the edges of these islands constitute sinks for intercalated atoms.

A. Pre-nucleation deposition-diffusion equation analysis

Prior to nucleation, rotational symmetry implies that $C_{\rm int}(\tilde{\boldsymbol{r}},\tilde{t}) = C_{\rm int}(\tilde{r},\tilde{t})$ depends only on the distance, $\tilde{r} = |\tilde{\boldsymbol{r}}|$, from the defect at $\tilde{\boldsymbol{r}} = 0$. Note that the Dirac delta function satisfies $\delta(\tilde{\boldsymbol{r}}) = \delta(\tilde{r})/(\pi\tilde{r})$, and the Laplacian satisfies $\nabla^2_{\tilde{\boldsymbol{r}}} = \frac{1}{\tilde{r}}\frac{\partial}{\partial\tilde{r}}(\tilde{r}\frac{\partial}{\partial\tilde{r}})$ in this 2D rotationally isotropic system. Then, $C_{\rm int}(\tilde{\boldsymbol{r}},\tilde{t})$ follows from analysis of the equation

$$\frac{\partial C_{\rm int}(\tilde{r},\tilde{t})}{\partial \tilde{t}} = \frac{1}{\tilde{r}}\frac{\partial}{\partial\tilde{r}}\left(\tilde{r}\frac{\partial C_{\rm int}(\tilde{r},\tilde{t})}{\partial\tilde{r}}\right) + \frac{\delta(\tilde{r})}{\pi\tilde{r}} \quad \text{for } 0 \leqslant r < \infty, \tag{4}$$

or from dropping the source term and adding the flux boundary condition described above at $\tilde{r} = \tilde{r}_d$. Mass conservation implies that $2\pi \int_0^\infty C_{int}(\tilde{r},\tilde{t})\tilde{r}d\tilde{r} = \tilde{t}$.

For the treatment retaining the delta function source (corresponding to the idealization of setting the defect radius to be exactly zero), the solution satisfies the additional scaling property $C_{int}(\tilde{r},\tilde{t}) = f(u)$, where $u \equiv \tilde{r}/\sqrt{\tilde{t}}$. Substitution into Eq. (4) yields the equation $-\frac{u}{2}\frac{df}{du} = \frac{1}{u}\frac{d}{du}(u\frac{df}{du}) + \frac{\delta(u)}{\pi u}$. Solution of this equation yields $f(u) = \frac{\pi}{4}\Gamma(0,\frac{u^2}{4})$, where $\Gamma(s,z)$ is the incomplete Gamma function, and $\Gamma(0,z) = E_1(z)$ corresponds to the exponential integral function. This solution of Eq. (4), and even more general problems with time-varying input, is known, although it is traditionally derived based on convolution with the fundamental solution to the diffusion equation [11]. Thus, for the (unscaled) intercalated atom density, one obtains

$$n_{int}(r,t) = \frac{J_{int}}{4\pi D_{int}}\Gamma\left(0,\frac{r^2}{4D_{int}t}\right) \quad \text{for } r_d = 0 \text{ (zero defect radius).} \tag{5}$$

From (5), one has that $n_{int}(r,t) \approx \frac{J_{int}}{2\pi D_{int}}\ln(\frac{1}{r})$ for $r \to 0$, as indicated above, and $n_{int}(r,t) \approx \frac{J_{int}t}{\pi r^2}\exp(\frac{-r^2}{4D_{int}t})$ for $r \to \infty$.

It should be noted that for the more realistic case of small finite defect radius, $\tilde{r}_d \ll 1$, solution of Eq. (4) with the source term replaced by the flux boundary condition at $\tilde{r} = \tilde{r}_d$ does not exactly satisfy the additional scaling property of the above paragraph, and no exact closed form solution is available. However, one expects that $C_{int}(\tilde{r},\tilde{t}) \approx f(\tilde{r}/\sqrt{\tilde{t}})$ is closely satisfied for small $\tilde{r}_d \ll 1$. In this case, accurate analysis of behavior is still readily assessed by numerical integration of diffusion equation with the appropriate boundary condition. Results obtained using the PDE-solver, PDSOLVE, in MAPLE [12] for $C_{int}(\tilde{r},\tilde{t})$ with $\tilde{r}_d = 0.05$ are shown in the inset of Fig. 2(a) for a sequence of increasing scaled times.

The central motivation for the above analysis of n_{int} is to provide an assessment of the nucleation kinetics for intercalated islands. Here, it is common to introduce a critical size i, where $i+1$ atoms are required to form a stable nucleus. Then $i = 1$ is referred to as irreversible island formation (since any pair of diffusing atoms which meet irreversibly form a stable dimer), and $i > 1$ corresponds to reversible island formation. In general, for a lateral unit cell area Ω for the intercalated layer, the local nucleation rate per unit area, k_{nuc}, has the form [1,3]

$$k_{nuc}(\boldsymbol{r},t) = k_{nuc}(r,t) = \sigma_i(\Omega n_{int})^{i+1}\frac{D_{int}}{\Omega^2}\exp(-\beta E_{b,i}). \tag{6}$$

Here, dimensionless $\sigma_i \sim 1$ is the capture number, and $E_{b,i} < 0$ is the binding energy for attractive atom-atom interactions of critical clusters of i atoms. From the scaling form of n_{int}, it is clear that $k_{nuc}(r,t)$ decreases monotonically with increasing r. See Fig. 2(a) for $i = 1$. However, the probability of nucleation between a distance r and $r + dr$ from the defect scales like $rk_{nuc}(r,t)dr$, which has a peak value for $r > 0$ [see Fig. 2(b) for $i = 1$]. The total nucleation rate is given

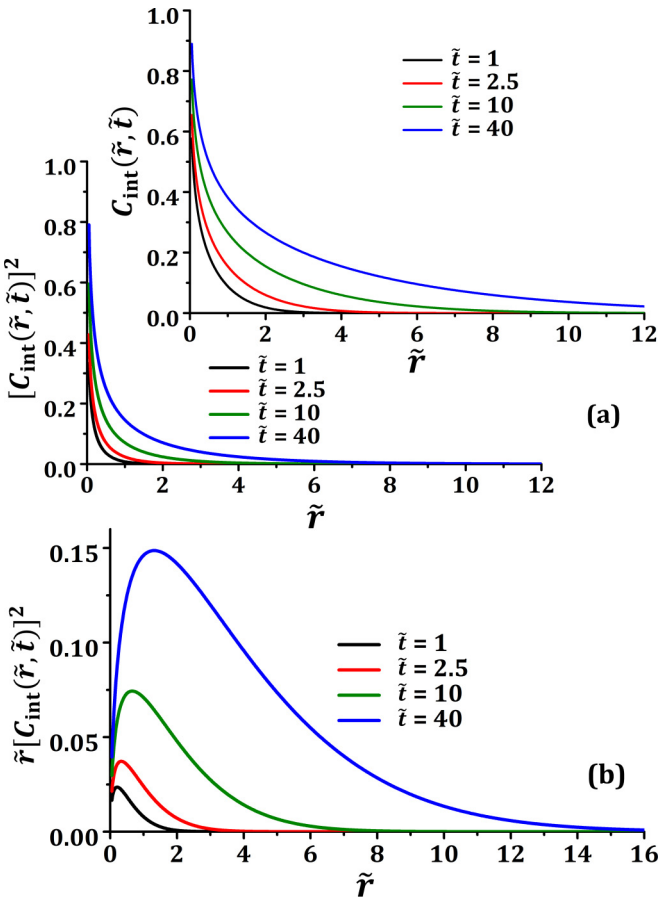

FIG. 2. Inset in (a): result of numerical analysis with $\tilde{r}_d = 0.05$ for $C_{int}(\tilde{r},\tilde{t})$. (a) The associated scaled nucleation rate per unit area. (b) The associated scaled nucleation rate per increment in radial distance from the defect.

by

$$K_{nuc}(t) = \iint_{\mathbf{R}^2} k_{nuc}(\boldsymbol{r},t)dr = 2\pi\int_0^\infty rk_{nuc}(r,t)dr$$
$$= 2\pi\sigma_i\left(\frac{\Omega J_{int}}{D_{int}}\right)^{i-1} J_{int}\exp(-\beta E_{b,i})$$
$$\times \int_0^\infty \tilde{r}[C_{int}(\tilde{r},\tilde{t})]^{i+1}d\tilde{r}\,. \tag{7}$$

Using $C_{int}(\tilde{r},\tilde{t}) \approx f(\tilde{r}/\sqrt{\tilde{t}})$ reveals that $K_{nuc}(t)$ increases linearly with time for all i. From $K_{nuc}(t)$, it is possible to assess the typical time, t_{nuc}, for nucleation of the first island from the condition $\int_0^{t_{nuc}} K_{nuc}(t)\,dt \approx 1$. We conclude that

$$J_{int}t_{nuc} \approx \frac{1}{\sqrt{\pi\sigma_i\int_0^\infty u[f(u)]^{i+1}du}}\exp\left(\frac{\beta E_{b,i}}{2}\right)\left(\frac{D_{int}}{\Omega J_{int}}\right)^{\frac{i-1}{2}}. \tag{8}$$

In the case of irreversible island formation, $i = 1$ where $E_{b,i} = 0$, Eq. (8) shows that t_{nuc} is independent of D_{int} and one has that $J_{int}t_{nuc} \sim 1$ is of order unity.

Next, we assess the consequence of the above results for t_{nuc} on the nucleation position. Using $C_{int}(\tilde{r},\tilde{t}) \approx f(\tilde{r}/\sqrt{\tilde{t}})$, the mean position for nucleation occurring specifically at time t is

given by

$$r_{\rm nuc}(t) = c_{\rm nuc}\sqrt{D_{\rm int}t}, \quad \text{where } c_{\rm nuc} = \frac{\int_0^\infty u^2\,[f(u)]^{i+1}\,du}{\int_0^\infty u\,[f(u)]^{i+1}\,du}. \tag{9}$$

Then, we determine the typical nucleation distance from the defect as

$$\langle r_{\rm nuc}\rangle = r_{\rm nuc}(t_{\rm nuc}) = c_{\rm nuc}\sqrt{D_{\rm int}t_{\rm nuc}} \approx \sqrt{\Omega}\left(\frac{D_{\rm int}}{\Omega J_{\rm int}}\right)^{\frac{i+1}{4}}, \tag{10}$$

so that $\langle r_{\rm nuc}\rangle \approx \sqrt{D_{\rm int}/J_{\rm int}}$ for $i = 1$.

B. Post-nucleation continuum deposition-diffusion equation analysis

Nucleation of the first island creates a sink for intercalated atoms within the gallery which will consequently greatly reduce the density of nearby intercalated atoms. To what extent does this inhibit the subsequent nucleation of additional intercalated islands? We argue that post-nucleation buildup of the overall intercalated adatom density, $n_{\rm int}(\boldsymbol{r},t)$, continues sufficiently strongly that nucleation of subsequent islands is persistent.

A comprehensive assessment of this behavior requires analysis of a boundary value problem for the deposition-diffusion equation Eq. (1) for $n_{\rm int}(\boldsymbol{r},t)$ with a point-source at $\boldsymbol{r} = 0$ in a more complicated geometry including an intercalated island (or islands) the periphery of which constitutes perfect sinks for intercalated atoms. Thus there is no longer rotational symmetry, and numerical analysis of the problem is required. Rather than a complete analysis of this problem, we just note that in the absence of island nucleation beyond the first island (and considering growth of this single island to be slow), the far-field value of $n_{\rm int}(\boldsymbol{r},t)$ would grow to a nonzero constant value. This value reflects a balance between gain of intercalated atoms due to input at $\boldsymbol{r} = 0$ and a loss due to aggregation with the single island. Given the tendency of $n_{\rm int}(\boldsymbol{r},t)$ to evolve towards this nonzero far-field value, it is clear that a second island must at some point be nucleated (most likely on the other side of the defect from the first island).

After the second island has nucleated, the far-field $n_{\rm int}(\boldsymbol{r},t)$ would tend to approach a substantially lower value than with just one island due to the stronger trapping effect for intercalated atoms of two islands over one island. Nonetheless, this value would still be nonzero, ensuring nucleation of a third island. The process continues where the increasing number of islands produces a tendency towards progressively lower but still nonzero far field values of $n_{\rm int}(\boldsymbol{r},t)$, and thus persistent but progressively slower subsequent nucleation. We have performed a precise numerical analysis using adaptive mesh refinement of the steady-state regime based on the scaled equation (3) for various island geometries where islands are a distance of order $\sqrt{D_{\rm int}/J_{\rm int}}$ from $\boldsymbol{r} = 0$ corresponding to $i = 1$. We thereby quantify the above mentioned progressive reduction in far-field densities (see the Appendix).

Finally, we remark that the typical pattern of nucleated island positions should involve the second island nucleating on the opposite side of the defect than the first as noted above, and then the third and fourth islands nucleating in the orthogonal direction. However, in a stochastic LG model for this process as described in Sec. III, large fluctuations in nucleation positions (and times) often disrupt this pattern. Furthermore, it is common that the island closest to the defect at later times is not the first island to be nucleated. These features are confirmed by our KMC simulations in Sec. IV.

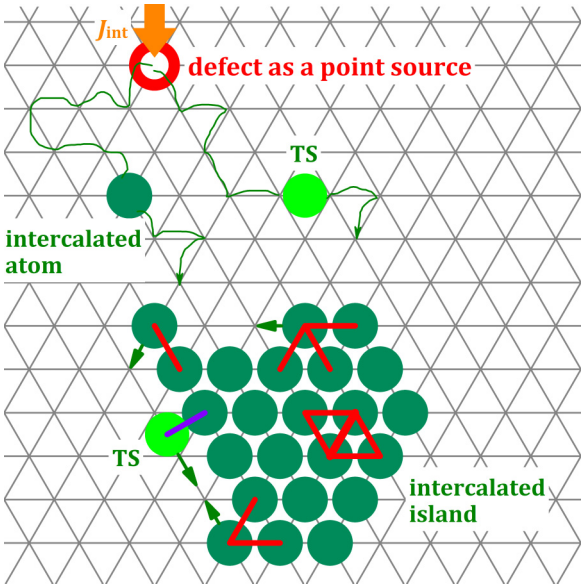

FIG. 3. Schematic of our stochastic LG model for intercalated island formation.

III. STOCHASTIC LATTICE-GAS MODEL OF NUCLEATION AND GROWTH

For intercalation of fcc or hcp metals in HOPG, one expects that single-layer or few-layer intercalated islands will have a hexagonal close-packed structure within each layer [4,5]. This structure, which is primarily driven by metal-metal intercalated atom interactions, naturally corresponds to the lowest-energy configuration in cases where the metal-graphene interaction is not dominant. Thus, to provide a more detailed characterization of intercalated island nucleation and growth incorporating this feature, we develop a suitable stochastic lattice-gas (LG) model incorporating a triangular lattice of sites (with coordination number six) on which intercalated atoms reside within the gallery. Since experimentally observed intercalated metal islands tend to have bulk structure, the lattice constant, a, will generally differ only slightly from the bulk metal lattice constant. The basic features of the model are as follows: atoms are injected at a single "point-source defect site" on the triangular lattice at rate $J_{\rm int}$. They initially undergo diffusion within the gallery as isolated atoms hopping between adjacent sites at rate $h_0 = \nu\exp(-\beta E_{\rm d})$ per direction, where $E_{\rm d}$ is the associated diffusion barrier, and ν is the attempt frequency. This prescription implies that $D_{\rm int} \propto a^2 h_0$. Thereafter, the intercalated atoms can potentially aggregate with other diffusing intercalated atoms or with existing intercalated islands (see Fig. 3). Thus one must prescribe the hopping rate, h, for a general local environment to account for attachment and detachment, edge diffusion, etc., as described below.

In our model, the hop rate (per direction) for any local environment is selected as $h = \nu \exp(-\beta E_{\rm act})$, where the activation barrier has the form $E_{\rm act} = E_{\rm d} + \Phi_{\rm TS} - \Phi_{\rm init}$ [13,14]. Here $\Phi_{\rm init}$ is the sum of all "conventional" lateral interactions, ω, for the hopping atom in the initial lattice site with other nearby atoms at lattice sites. $\Phi_{\rm TS}$ is the sum of "unconventional" interactions, ϕ, for the hopping atom at the transition state (TS) (roughly midway between adjacent lattice sites) with other atoms at nearby lattice sites. All these interactions correspond primarily to direct interactions for the systems of interest here. For terrace diffusion, one has that $\Phi_{\rm TS} = \Phi_{\rm init} = 0$, thereby recovering $E_{\rm act} = E_{\rm d}$.

A simple but reasonable prescription includes only (i) short-range conventional pair attractions, $\omega_{\rm p} = -\varepsilon$ with $\varepsilon > 0$ for nearest-neighbor atoms separated by a lattice constant, a, and (ii) short-range unconventional pair attractions, $\phi_{\rm p}$, of comparable magnitude for an atom at a TS separated by roughly $\sqrt{3}a/2$ from a nearby atom at a lattice site (cf. [13,14]). Model behavior will be similar for any comparable choice of $\omega_{\rm p}$ and $\phi_{\rm p}$, but here we set $\phi_{\rm p} = -\varepsilon$ for simplicity and to reduce the number of model parameters. Then, for edge diffusion, $\Phi_{\rm TS} = -\varepsilon$ always applies, but there are different possible values for $\Phi_{\rm init}$. These include $\Phi_{\rm init} = -\varepsilon$ for a singly coordinated edge atom at the corner of an island, $\Phi_{\rm init} = -2\varepsilon$, for a doubly coordinated isolated edge atom at a straight step edge, $\Phi_{\rm init} = -3\varepsilon$ for a triply-coordinated kink atom, and $\Phi_{\rm init} = -4\varepsilon$ for an atom embedded in a straight step edge (see Fig. 3). Thus one has $E_{\rm act} = E_{\rm e} = E_{\rm d} + \varepsilon$ for diffusion along a straight edge. This same barrier applies for hopping from the edge to a corner site, so there is no additional kink Ehrlich-Schwoebel (ES) barrier, and also for incorporation at a kink site. There is a higher barrier $E_{\rm act} = E_{\rm d} + 2\varepsilon$ to hop from a kink to an edge site. For a singly-bonded corner atom, the barrier to hop back to a doubly-coordinated edge site of $E_{\rm act} = E_{\rm d}$ is lower than the barrier to detach from the island of $E_{\rm act} = E_{\rm d} + \varepsilon$, i.e., detachment is inhibited relative to corner-to-edge hopping. One can show that the effective barrier for detachment of an isolated edge atom from an island via a corner site is $E_{\rm det} = E_{\rm d} + 2\varepsilon$, which equals the barrier for direct detachment from the step edge. Barriers for detachment of higher-coordinated atoms either directly or via corner sites are naturally higher.

The above prescription of kinetics actually provides a reasonable description of fcc (111) metal homoepitaxial systems, in marked contrast to standard "initial value approximation" or bond-breaking prescriptions [3]. In these systems, $E_{\rm e}$ significantly exceeds $E_{\rm d}$, kink ES barriers are small compared to $E_{\rm e}$, and corner-to-edge hopping is preferred over detachment [15,16]. As an aside, the above model can be refined in various ways. For example, by incorporating conventional repulsive triangular trio interactions, $\omega_{\rm t} = \delta$, where we expect that $\varepsilon \gg \delta > 0$ [17], one can reduce the edge diffusion barrier to $E_{\rm e} = E_{\rm d} + \varepsilon - \delta$. Finally, we emphasize, however, that the above model is idealized, and that actual diffusion processes and intercalated island structures within the gallery are more complex and system specific. For example, atom diffusion may be characterized by hopping between multiple stable local adsorption sites, but such fine details do not affect the key features of nucleation and growth. Also island structure can be multilayer versus single layer. However, our goal here is just to reasonably describe shape relaxation during growth for hexagonal close-packed intralayer structures in the presence of a localized source of atoms.

Next, we comment further on basic aspects of model behavior. Reversibility in island nucleation and growth impacts basic behavior (cf. Sec. II A and Ref. [3]). The degree of reversibility increases with the ratio of the rate for dissociation of a dimer, $h_{\rm diss,2} = h_0 \exp(-\beta\varepsilon)$ to the rate of aggregation, $h_{\rm agg} = \varphi J_{\rm int}$ of intercalated atoms with a just-formed dimer (or with the subsequent island), where φ denotes the fraction of intercalated atoms aggregating with the dimer or island. Irreversibility requires that

$$\frac{h_{\rm diss,2}}{h_{\rm agg}} = \frac{h_0}{\varphi J_{\rm int}} \exp(-\beta\varepsilon) \ll 1 \quad \text{for } i = 1. \tag{11}$$

Thus increasing T or decreasing ε induces a transition to a regime with $i > 1$. As the rate of dissociation of atoms from triangular trimers, $h_{\rm diss,3} = h_0 \exp[-\beta(2\varepsilon + \delta)]$, is substantially lower than $h_{\rm diss,2}$ for $\delta \ll \varepsilon$, there should be a well-defined regime with $i = 2$ when $h_{\rm diss,2}/h_{\rm agg} > 1$ but $h_{\rm diss,3}/h_{\rm agg} \ll 1$. In fact, such a regime is generally expected in fcc (111) metal homoepitaxy corresponding to stable triangular trimers [18,19]. Further increasing T or decreasing ε naturally leads to a transition out of $i = 2$ to a regime with $i > 2$.

Regarding growth shape evolution for the intercalated islands, very facile edge diffusion should produce quasiequilibrated hexagonal shapes centered on the nucleation site. Less facile edge diffusion will produce nonequilibrium possibly fractal shapes with growth biased back towards the defect reflecting a greater flux of diffusing atoms on that side. Let L denote the linear island size. Then, shape equilibration or even compactification requires the characteristic time, $\tau_{\rm edge} \sim L^2/h_{\rm e}$, for edge atoms to traverse the island perimeter (to access higher-coordinated incorporation sites) be significantly shorter than the time $\tau_{\rm agg} = 1/h_{\rm agg}$, between aggregation events [20,21]. Note that for the basic model with only pair interactions, dimer dissociation and edge diffusion rates are equal, i.e., $h_{\rm diss,2} = h_{\rm e}$. Thus the condition for the transition from irreversible to reversible island growth roughly corresponds to that for the transition from compact to irregular island shapes with $L = O(1)$, i.e., irreversible island formation would be associated with irregular islands.

IV. KMC SIMULATION RESULTS FOR THE STOCHASTIC LATTICE-GAS MODEL

Routine KMC simulation analysis of the basic stochastic lattice-gas model (with $\omega_{\rm p} = \phi_{\rm p} = -\varepsilon$ and $\delta = 0$) can be utilized to precisely characterize the overall island nucleation and growth process, including the morphologies and arrangement of growing islands. Here, we also exploit the versatility of KMC by performing tailored simulations to quantify specific detailed aspects of the nucleation process which are of interest.

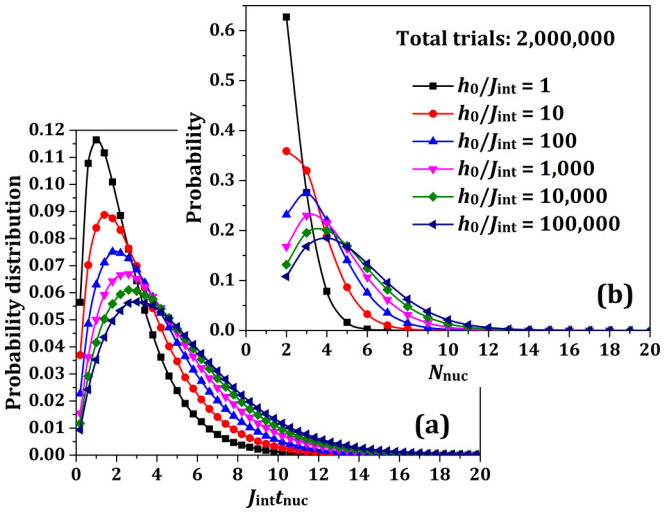

FIG. 4. (a) Normalized distribution of nucleation times for $i = 1$. Data are binned with a bin width of $J_{\rm int}\Delta t_{\rm nuc} = 0.4$. (b) Normalized distribution of the number of intercalated atoms upon nucleation of the first island for $i = 1$. Results are shown for various $h_0/J_{\rm int}$ indicated.

A. Nucleation of the first island for $i = 1$

We first utilize KMC simulation to provide an efficient and precise characterization of various basic aspects of the nucleation of the first island for $i = 1$. To this end, we run the simulation until the first nucleation event, i.e., until a pair of intercalated atoms reach adjacent sites to form a dimer. The simulation is then stopped and we record the nucleation time, $t_{\rm nuc}$, the nucleation distance from the defect, $r_{\rm nuc}$, and also the number of intercalated atoms, $N_{\rm nuc}$, at the time of nucleation. Here the nucleation position is defined as the midpoint of the dimer. The results are independent of the value of ε. Collecting statistics from 2 000 000 such simulation trials gives precise information of the distributions for the above quantities. The simulations were run for a broad range of values of $h_0/J_{\rm int}$ to assess the degree of convergence to limiting behavior as $h_0/J_{\rm int} \to \infty$.

The analysis from Sec. III suggests that the $t_{\rm nuc}$ distribution should have a mean value of the order $1/J_{\rm int}$. Thus, in Fig. 4(a), we plot the normalized distribution of values of $J_{\rm int}t_{\rm nuc}$, which depends only on $h_0/J_{\rm int}$ and which slowly approaches a well-defined limiting monomodal shape for increasing $h_0/J_{\rm int}$. As anticipated in Sec. III, this distribution is broad. The mean value $\langle t_{\rm nuc}\rangle$ of $t_{\rm nuc}$ satisfies $J_{\rm int}\langle t_{\rm nuc}\rangle = 2.49$, 3.16, 3.76, 4.26, 4.69, and 5.07 for $h_0/J_{\rm int} = 1$, 10, ..., and 100 000, respectively. Next, we consider the (discrete) distribution of the number of intercalated atoms, $N_{\rm nuc}$, at the time of nucleation of the first island, which also depends solely on $h_0/J_{\rm int}$. From the results shown in Fig. 4(b), the form of this distribution also approaches a limiting monomodal shape for increasing $h_0/J_{\rm int}$, and also mimics that for the distribution for $J_{\rm int}t_{\rm nuc}$. As already indicated in Sec. II, it is quite common that there are more than 2 intercalated atoms at the time of nucleation of the first island. Indeed, one finds that $\langle N_{\rm nuc}\rangle$ closely matches $J_{\rm int}\langle t_{\rm nuc}\rangle$. The similarity between the distributions for $N_{\rm nuc}$ and $J_{\rm int}t_{\rm nuc}$ derives from the feature that these quantities are strongly linearly correlated. This feature is demonstrated from

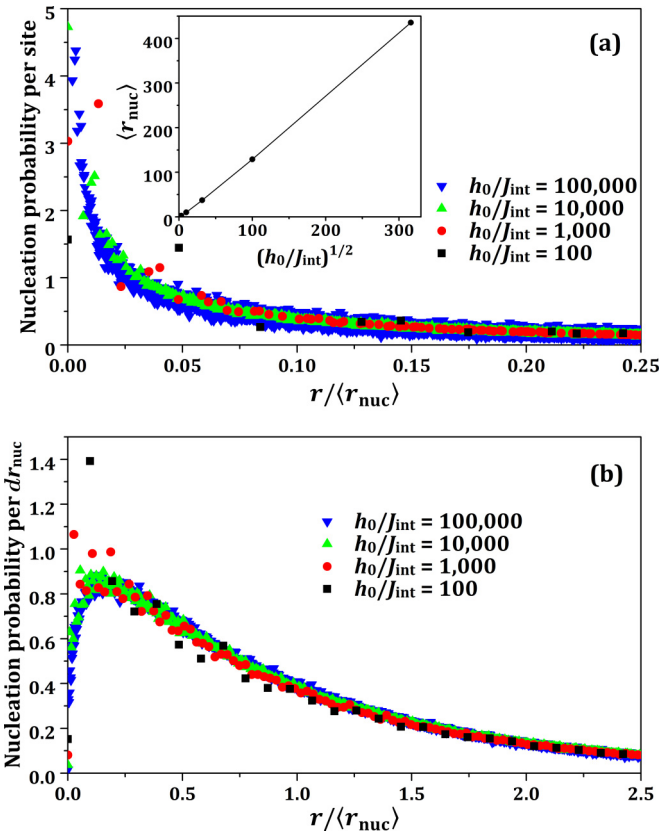

FIG. 5. Distributions vs scaled distance from the defect with $i = 1$ for (a) nucleation probability per site; (b) nucleation probability per increment of radial distance. Data are binned with bin width of $\Delta r_{\rm nuc} = 1$. Inset in (a): $\langle r_{\rm nuc}\rangle$ vs $(h_0/J_{\rm int})^{1/2}$.

a finer-level analysis. For example, if $\langle t_{\rm nuc}(N_{\rm nuc})\rangle$ denotes the mean nucleation time for a specific $N_{\rm nuc}$, we find that $\langle t_{\rm nuc}(N_{\rm nuc})\rangle$ increases near-linearly as a function of $N_{\rm nuc}$. For $\frac{h_0}{J_{\rm int}} = 100000$, one has that $J_{\rm int}\langle t_{\rm nuc}(N_{\rm nuc})\rangle \approx 1.93$, 2.94, 3.97, 4.99, 6.01, and 7.06 for $N_{\rm nuc} = 2$, 3, ..., and 7, respectively.

Next, we consider the $r_{\rm nuc}$ distribution which depends exclusively on $h_0/J_{\rm int}$ with mean scaling like $\sqrt{h_0/J_{\rm int}}$. The inset in Fig. 5(a) shows data for $\langle r_{\rm nuc}\rangle = 0.59$, 2.57, 10.3, 37.4, 129, and 435 lattice constants for $h_0/J_{\rm int} = 1$, 10, 100, 1000, and 10000, respectively, exhibiting approximate scaling $\langle r_{\rm nuc}\rangle \approx 1.3\sqrt{h_0/J_{\rm int}}$. This broad range of $\langle r_{\rm nuc}\rangle$ may not be realized in experiment (e.g., $\langle r_{\rm nuc}\rangle \sim 40$ for Dy deposition at 800 K), but our goal here is fundamental analysis of scaling. The main frame of Fig. 5(a) shows the distribution of scaled nucleation distances from the defect, based on the nucleation probability per site. Also, values for symmetry-equivalent sites, the same distance from the defect have been averaged to reduce statistical noise. Scaling of the vertical axis is chosen to appropriately normalize the distribution revealing collapse of the curves for various larger $h_0/J_{\rm int}$. Figure 5(b) shows the nucleation probability per increment of scaled radial distance from the defect. This quantity naturally has a different form from the nucleation probability per site as the number of sites within an increment of distance from the defect increases linearly with distance. One might compare Figs. 5(a) and 5(b) with the similar forms in Figs. 2(a) and 2(b), although

we caution that the quantities are different in detail. Figure 2 refers to nucleation of the first island at specific times, whereas Fig. 5 accumulates statistics for a range of times as quantified in Fig. 4(a).

B. Nucleation of the first island for $i = 2$

As noted in Sec. III B, one expects to have a well-defined regime of island nucleation with $i = 2$ for a range of T which is slightly too high, or interactions ε which are slightly too weak, to support irreversible island formation. As also indicated in Sec. III, compact intercalated islands, often observed in experiment, will most naturally occur for $i > 1$. Analogous to $i = 1$, we present KMC results for $i = 2$ providing a detailed characterization of $t_{\rm nuc}$, $r_{\rm nuc}$, and $N_{\rm nuc}$ for nucleation of the first island. To be more precise, we define this nucleation event as the first formation of a triangular trimer (at which point the simulation is terminated), noting that other linear and bent configurations of trimers are no more stable than dimers. Correspondingly, we define the nucleation position to be the center of the triangular trimer. As an aside, we discard trials where an impinging atom lands upon an isolated intercalated atom still at the defect site.

We emphasize that KMC simulation is more demanding for $i = 2$ than $i = 1$ (just as for conventional nucleation with uniform deposition flux where KMC quickly becomes prohibitive for larger i) [3]. Also behavior does now depend on the value of ε (chosen in a suitable range to ensure triangular trimers but not dimers are stable so that $i = 2$). Our primary interest is in assessing the basic scaling behavior for $i = 2$ for comparison with the predictions of analytic theory in Sec. II A. Thus, we consider the limiting case setting $\varepsilon = 0$, but regard triangular trimers and larger islands as stable. Choosing small $\varepsilon > 0$ would enhance the lifetime of (unstable) dimers, thus enhancing nucleation, but this should not change the scaling properties. We collect statistics from 2 000 000 simulation trials to determine distributions for key quantities of interest. The simulations were run for a range of values of $h_0/J_{\rm int}$, which is more limited than for $i = 1$ due to the above-mentioned additional computational cost.

The distribution of values of $J_{\rm int}t_{\rm nuc}$ again depends only on $h_0/J_{\rm int}$, but in contrast to $i = 1$, the mean value now depends strongly on this parameter. Specifically, we find that $J_{\rm int}\langle t_{\rm nuc}\rangle \approx 6.19, 13.37$, and 35.91 for $h_0/J_{\rm int} = 1, 10$, and 100, respectively (values much larger than those for $i = 1$). This behavior is consistent with the scaling $J_{\rm int}\langle t_{\rm nuc}\rangle \sim (h_0/J_{\rm int})^{1/2}$ proposed for $i = 2$ in Sec. II A noting that $\langle t_{\rm nuc}\rangle$ increases by a factor of 2.69 as $h_0/J_{\rm int}$ increases from 10 to 100, being reasonably close to $10^{1/2} \approx 3.16$. Consequently, in Fig. 6(a), we must plot the rescaled distribution for $t_{\rm nuc}/\langle t_{\rm nuc}\rangle$ for various $h_0/J_{\rm int}$ in order to achieve collapse of these distributions. The (discrete) distribution of the number of intercalated atoms, $N_{\rm nuc}$, upon nucleation which also has the feature that the mean strongly depends on $h_0/J_{\rm int}$ with $\langle N_{\rm nuc}\rangle = 5.63$, 13.14, and 35.83 for $h_0/J_{\rm int} = 1, 10$, and 100, respectively (cf. smaller $i = 1$ values). Thus, in Fig. 6(b), we plot the rescaled distribution as a function of $N_{\rm nuc}/\langle N_{\rm nuc}\rangle$ for various $h_0/J_{\rm int}$ to achieve collapse of these distributions. The similarity between the distributions for $N_{\rm nuc}$ and $J_{\rm int}t_{\rm nuc}$ again derives from the feature that $J_{\rm int}\langle t_{\rm nuc}(N_{\rm nuc})\rangle$ increases near-linearly as a function of

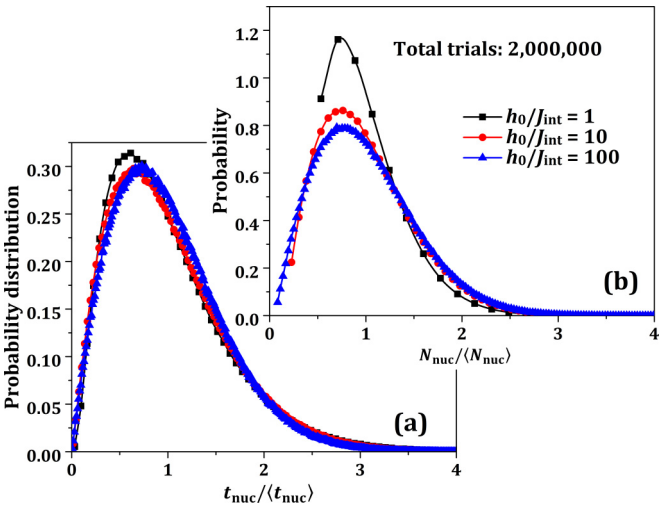

FIG. 6. (a) Normalized distribution of nucleation times for $i = 2$ for $h_0/J_{\rm int} = 1$, 10, and 100. Data are binned with bin width of $J_{\rm int}\Delta t_{\rm nuc} = 0.4$. (b) Distribution of the number of intercalated atoms upon nucleation of the first island.

$N_{\rm nuc}$. For $h_0/J_{\rm int} = 100$, one has that $J_{\rm int}\langle t_{\rm nuc}(N_{\rm nuc})\rangle \approx 2.03$, 3.06, 4.10, 5.08, and 6.07, for $N_{\rm nuc} = 3$, 4, 5, 6, and 7, respectively.

Next, we consider the $r_{\rm nuc}$ distribution which depends exclusively on $h_0/J_{\rm int}$. However, in contrast to $i = 1$, the mean value $\langle r_{\rm nuc}\rangle = 1.16, 4.85$, and 24.68 for $h_0/J_{\rm int} = 1, 10$, and 100, respectively, does not scale like $\langle r_{\rm nuc}\rangle \sim (h_0/J_{\rm int})^{1/2}$ The behavior is rather consistent with the scaling $\langle r_{\rm nuc}\rangle \sim (h_0/J_{\rm int})^{3/4}$ suggested in Sec. II A for $i = 2$, noting that $\langle r_{\rm nuc}\rangle$ increases by a factor of 5.09 as $h_0/J_{\rm int}$ increases from 10 to 100, being reasonably close to $10^{3/4} \approx 5.62$. Figure 7 shows the nucleation probability per increment of scaled radial distance from the defect. The emergence of a peaked form to this distribution is clear analogous to Fig. 5(b) for $i = 1$, although our limited statistics for $i = 2$ and the limited range

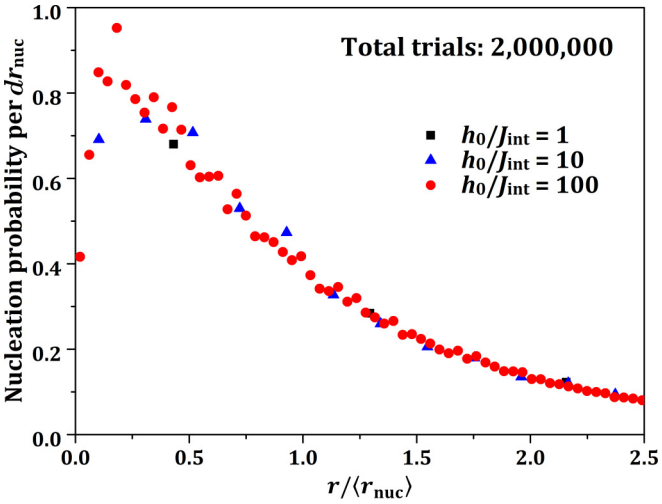

FIG. 7. Distribution of nucleation probability per increment of radial distance vs scaled distance from the defect for $i = 2$. Binned data are shown with a bin width of $\Delta r_{\rm nuc} = 1$.

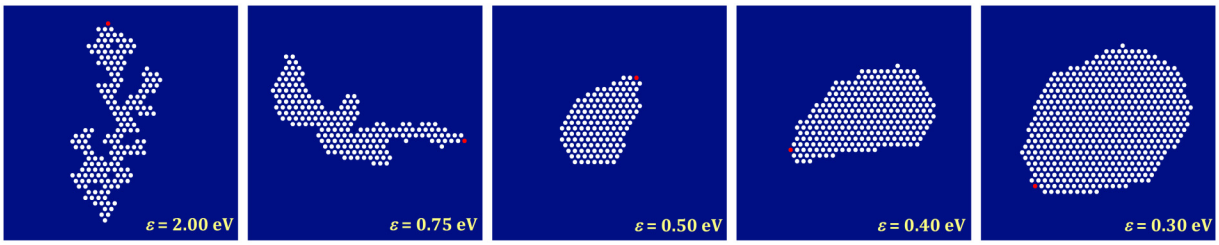

FIG. 8. Examples from KMC simulation of intercalated island growth shapes and directional bias for $h_0/J_{\text{int}} = 4000$, and $\varepsilon = 2.00$, 0.75, 0.50, 0.40, and 0.30 eV (left to right) at $T = 800$ K. White dots denote intercalated atoms, and the red dot gives the location of the defect. Image size: $36a \times 36a$.

of h_0/J_{int} means that we cannot capture the limiting form of this distribution.

C. Island growth shapes and nucleation of subsequent islands

Next, we present results from our KMC simulations of the overall nucleation and growth process. Specifically, we focus on the shape of the island closest to the defect. Growth of this island is biased back to the defect, and thus upon reaching the defect it ultimately blocks further injection of atoms to the gallery. Figure 8 shows a few examples for fixed $h_0/J_{\text{int}} = 4000$ and various ε of the shapes of such islands upon reaching the defect (indicated by a red dot). We have noted that island formation is irreversible and the shape instability is prominent for large ε, but island formation becomes reversible and shapes more compact for smaller ε. Applying the criteria of Sec. III B, we estimate that the transition at 800 K from $i = 1$ and $i = 2$ will occur as ε drops below $\varepsilon_{1\to 2} \approx 0.75$ eV (for our choice of $h_0/J_{\text{int}} = 4000$ and using $\varphi = 0.1$). Likewise, the transition from $i = 2$ to $i > 2$ will occur as ε drops below $\varepsilon_{2\to 3+} \approx 0.37$ eV.

For large $\varepsilon = 2.00$ and 0.75 eV, island formation is strongly irreversible (no dimers are observed to dissociate in the simulations), and there is a pronounced shape instability leading to fractal islands with a strong preference for growth back towards the defect. For $\varepsilon = 0.50$ and 0.40 eV, island formation is reversible with many dimers observed to dissociate in the simulations. However, dissociation of triangular trimers is very rare even at $\varepsilon = 0.40$ eV, so one has $i = 2$. Island shapes are compact although strongly distorted from equilibrium hexagonal shapes. For $\varepsilon = 0.30$ eV, dissociation of triangular trimers and also detachment of doubly-coordinated atoms from larger islands is observed in the simulations, so one has that $i > 2$. Island shapes are closer to equilibrated.

Finally, we show an example of simulation results illustrating the array of multiple islands nucleated for $h_0/J_{\text{int}} = 4000$, $\varepsilon = 0.40$ eV, and $T = 800$ K. In the images of Fig. 9, we have labeled the islands in order of their nucleation. The situation shown here is common where the closest island to the defect is not the first nucleated (and often not the second). However, we argue that the basic scaling behavior for the mean nucleation time and distance from the defect which applies for the first island nucleated should also apply for subsequent islands.

V. DISCUSSION AND APPLICATION TO SPECIFIC SYSTEMS

Nucleation and growth of near-surface intercalated islands mediated by diffusion of intercalated atoms fed by an isolated point-source-like defect has received little attention compared to the extensive analyses for surface islands fed by a uniform deposition flux [1,3]. The current study provides a comprehensive characterization for the nucleation process of intercalated islands combining both analytic theory and KMC simulation of a stochastic lattice-gas model. In particular, the analytic treatment indicates nontrivial scaling behavior of key quantities characterizing nucleation as a function of critical size. These predictions are confirmed by the KMC studies.

The motivation for the formulation of our model for nucleation and growth of intercalated islands was provided by recent experimental studies on this topic [4,5]. In particular, scanning tunneling microscopy (STM) observations for intercalated Dy islands on damaged HOPG guided model formulation. For this system, large intercalated islands of about 15 to 40 nm in linear dimension were formed by deposition of about 0.1 ML of Dy at 800 K. A particular feature revealed by the STM images is that these intercalated islands are often decorated by a surface island protruding above the top layer of HOPG near

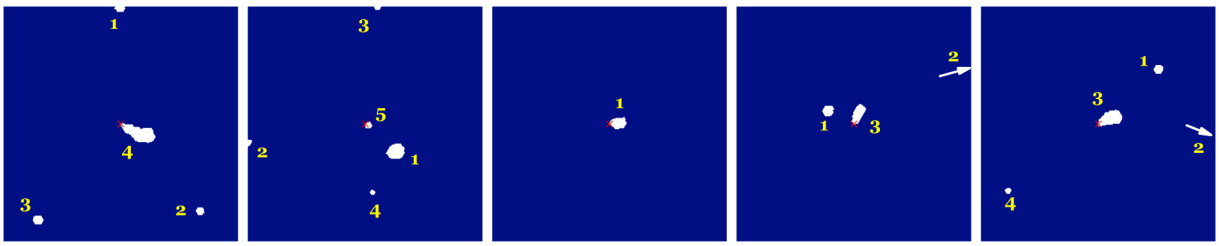

FIG. 9. KMC simulation images (size: $110a \times 110a$) from five independent trials, showing multiple islands (white) nucleated around the defect (red ×) for $h_0/J_{\text{int}} = 4000$, $\varepsilon = 0.40$ eV, and $T = 800$ K. Islands are labeled in order of nucleation from 1 to 2 to 3 to .... An arrow indicates the labelled island nucleates far from the defect (beyond the image size).

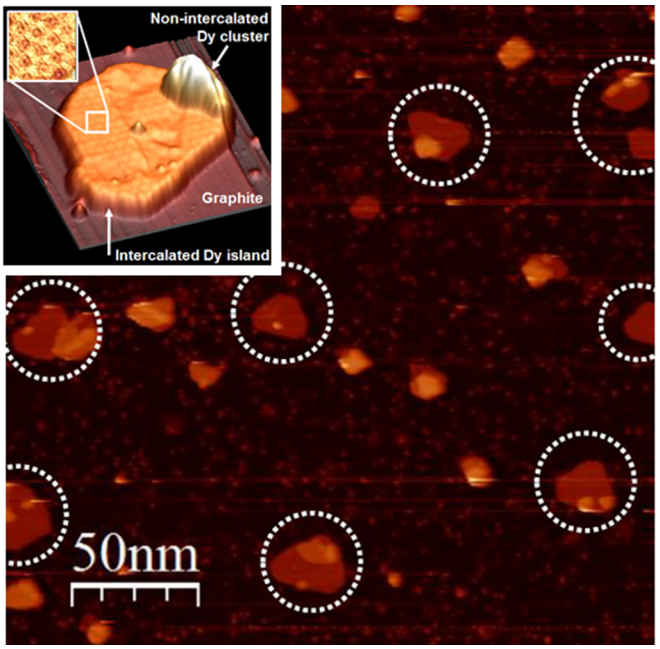

FIG. 10. Intercalated Dy islands (circled) as well as surface Dy islands for deposition of Dy on Ar^+-sputtered HOPG at 800 K. Brighter regions on the intercalated islands correspond to on-top surface islands indicating the location of the defect, which primarily feeds intercalated island growth. The intercalated island on the middle right has no on-top island and has plausibly nucleated far from a defect and not grown back to that defect.

their periphery (see Fig. 10 and Ref. [5] for further discussion of experiments). This suggests that intercalated islands are generally nucleated at some distance from isolated pointlike defects, and subsequently exhibit biased growth back towards the defect. Upon their periphery reaching the defect, injection of further surface adatoms is presumably blocked or at least strongly inhibited. This limits further lateral growth of the intercalated islands, and initiates growth of a multilayer surface island extending above the top layer of HOPG. This surface island is generally located near the periphery of the intercalated island. This feature is consistent with our proposed model.

Our generic model for nucleation and growth of intercalated islands is not geared to a specific system, for which appropriate refinements should be made. For example, for Dy/HOPG, intercalated islands are three atomic layers rather than a single atomic layer in thickness or height [5]. The model can be adjusted to incorporate this feature. Preliminary DFT analysis for this system does indicate the presence of a significant additional barrier for adatoms to enter the gallery through a defect. This barrier decreases with increasing defect size analogous to the study for Cs [4]. Our DFT analysis also indicated a diffusion barrier for intercalated atoms between the top two graphene layers of perfect HOPG, which is lower than might be anticipated from interpretation of STM data in the context of our modeling. However, the presence of many small surface islands could induce a higher effective barrier. Estimation of the effective diffusion rate for intercalated atoms might be obtained from Eq. (7) using experimental observations or estimates for $\langle r_{\rm nuc}\rangle$ and $J_{\rm int}$. Detailed system-specific modeling for Dy/HOPG and other systems will be pursued elsewhere.

Finally, we remark that general interest in the formation of near-surface intercalated islands is expected given the opportunity to modify surface properties for applications such as catalysis and magnetism. Of particular appeal is the possibility to protect metallic surface nanostructures from degradation under operation due to being covered by one or more graphene layers for intercalation in HOPG.

ACKNOWLEDGMENTS

Y.H., A.L.-R., Y.Z., M.K., M.C.T., C.-Z.W., and P.A.T. were supported for this work by the U. S. Department of Energy (USDOE), Office of Science, Basic Energy Sciences (BES), Materials Sciences and Engineering Division. J.W.E. was supported by the USDOE BES Division of Chemical Sciences, Geosciences, and Biosciences for development of the analytic theory and the lattice-gas modeling. Research was performed at the Ames Laboratory, which is operated by Iowa State University under Contract No. DE-AC02-07CH11358. Y.Z.'s participation in experimental studies motivating this analysis was supported by the China Scholarship Council. C.-J.W. performed the numerical 2D PDE analysis for which he was partially supported by the Ministry of Science and Technology (MOST) of Taiwan 105-2115-M-011-MY2.

APPENDIX: FAR-FIELD DENSITY OF INTERCALATED ATOMS VERSUS NUMBER OF ISLANDS.

Here, we consider instructive boundary value problems (BVPs) for the steady-state diffusion equation (3) with the scaled intercalated atom density, $C_{\rm int}(\tilde{\boldsymbol{r}},\tilde{t})$, replacing the delta-function source with the flux boundary condition, $-2\pi\tilde{r}\,\frac{\partial C_{\rm int}}{\partial \tilde{r}} = 1$, at $\tilde{r} = |\tilde{\boldsymbol{r}}| = \tilde{r}_{\rm d} \ll 1$. In addition, we introduce one or more island "sinks" imposing Dirichlet boundary conditions, $C_{\rm int} = 0$, on their edges. We perform a numerical analysis of this BVP exploiting adaptive mesh refinement methods and using COMSOL [22] software. However, this requires analysis for a finite spatial domain, so we impose an additional zero-flux boundary condition, $\frac{\partial C_{\rm int}}{\partial \tilde{r}} = 0$, on a large circle $\tilde{r} = |\tilde{\boldsymbol{r}}| = \tilde{R} \gg 1$, and solve the Laplace equation on the domain $\tilde{r}_{\rm d} \ll \tilde{r} \ll \tilde{R}$ and also exterior to the prescribed islands, see Fig. 11.

Our goal in this analysis is to determine the variation in the far-field steady-state value of $C_{\rm int}$ in the limit as $\tilde{R} \to \infty$. For $\tilde{r}_{\rm d} = 0.1$, the rotationally-averaged far-field values of $C_{\rm int}$ at $\tilde{\boldsymbol{r}} = \tilde{\boldsymbol{R}}$ are given by 0.2210, 0.05857, and 0.008638 for 1, 2, and 4 islands, respectively, for $\tilde{R} = 1024$ (not much different from values of 0.2321, 0.05917, and 0.008683, respectively, for $\tilde{R} = 4$). For $\tilde{r}_{\rm d} = 0.01$, the rotationally-averaged far-field values of $C_{\rm int}$ at $\tilde{\boldsymbol{r}} = \tilde{\boldsymbol{R}}$ change only slightly to 0.2194, 0.05857, and 0.008637 for 1, 2, and 4 islands, respectively, for $\tilde{R} = 1024$. Thus the strength of islands as a sink for intercalated atoms greatly increases the number of such islands as reflected by the dramatic decrease in the far-field value of $C_{\rm int}$. This in turn greatly reduces the probability of nucleation beyond the islands closest to the defect, a feature seen in the simulations. Finally, we note that the strength of the island sinks naturally also depends on their radii. Specifically, the far-field $C_{\rm int}$ increasing logarithmically with decreasing island radius.

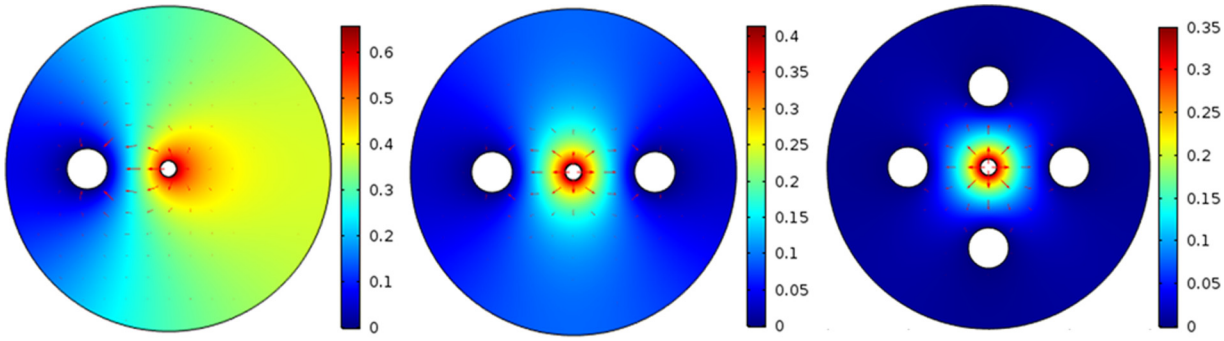

FIG. 11. COMSOL analysis of the steady-state deposition-diffusion equation with a localized source at the origin and perfect sinks at the periphery on one or more islands. Results shown are for a scaled radius of 0.1 for the source at the origin, scaled radii for all islands of 0.25, where island centers are a scaled distance 1 from the origin, and an outer radius of 2 where a zero-flux condition is imposed. Legends indicate the scaled density.

[1] J. A. Venables, G. D. T. Spiller, and M. Hanbücken, Nucleation and growth of thin films, Rep. Prog. Phys. **47**, 399 (1984).

[2] T. Michely and J. Krug, *Islands, Mounds and Atoms* (Springer, Berlin, 2004).

[3] J. W. Evans, P. A. Thiel, and M. C. Bartelt, Morphological evolution during epitaxial thin film growth: Formation of 2D islands and 3D mounds, Surf. Sci. Rep. **61**, 1 (2006).

[4] M. Büttner, P. Choudhury, J. K. Johnson, and J. T. Yates, Vacancy clusters as entry ports for cesium intercalation in graphite, Carbon **49**, 3937 (2011).

[5] Y. Zhou, A. Lii-Rosales, M. Kim, M. Wallingford, D. Jing, M. C. Tringides, C.-Z. Wang, and P. A. Thiel, Defect-mediated, thermally-activated encapsulation of metals at the surface of graphite (unpublished).

[6] *Graphite Intercalation Compounds I*, edited by H. Zabel and S. A. Solin, Springer Series in Materials Science Vol. 14, (Springer, Berlin, 1990).

[7] S. H. A. Axdal and D. D. L. Chung, A theory for the kinetics of intercalation of graphite, Carbon **25**, 377 (1987).

[8] R. B. Smith, E. Khoo, and M. Z. Bazant, Intercalation kinetics in multiphase-layered materials, J. Phys. Chem. C **121**, 12505 (2017).

[9] E. J. Kwolek, H. Lei, A. Lii-Rosales, M. Wallingford, Y. Zhou, C.-Z. Wang, M. C. Tringides, J. W. Evans, and P. A. Thiel, Adsorption of dysprosium on the graphite (0001) surface: Nucleation and growth at 300 K, J. Chem. Phys. **145**, 211902 (2016).

[10] D. Appy, H. Lei, C.-Z. Wang, M. C. Tringides, D.-J. Liu, J.W. Evans, and P. A. Thiel, Transition metals on the (0001) surface of graphite: Fundamental aspects of adsorption, diffusion, and morphology, Prog. Surf. Sci. **89**, 219 (2014).

[11] F. Treves, *Basic Linear Partial Differential Equations* (Academic, New York, 1975) presents the basics of the relevant analysis of initial value problems utilizing fundamental solutions. D. Gurarie, https://case.edu/artsci/math/gurarie/classes/445/heat-diff.pdf specifically analyzes the diffusion equation with a point source.

[12] E. S. Cheb-Terrab and K. von Bülow, A computational approach for the analytical solving of partial differential equations, Comp. Phys. Comm. **90**, 102 (1995).

[13] Y. Han, B. Ünal, and J. W. Evans, Formation of a Novel Ordered Ni_3Al Surface Structure by Codeposition on NiAl(110), Phys. Rev. Lett. **108**, 216102 (2012).

[14] Y. Han, D.-J. Liu, and J. W. Evans, Real-time ab initio KMC simulation of the self-assembly and sintering of bimetallic epitaxial nanoclusters: Au + Ag on Ag(100), Nano Lett. **14**, 4646 (2014).

[15] A. Bogicevic, J. Strömquist, and B. I. Lundqvist, Low-Symmetry Diffusion Barriers in Homoepitaxial Growth of Al(111), Phys. Rev. Lett. **81**, 637 (1998).

[16] E. Cox, M. Li, P.-W. Chung, C. Ghosh, T. S. Rahman, C. J. Jenks, J. W. Evans, and P. A. Thiel, Temperature dependence of island growth shapes during submonolayer deposition of Ag on Ag(111), Phys. Rev. B **71**, 115414 (2005).

[17] T. J. Stasevich, T. L. Einstein, and S. Stolbov, Extended lattice gas interactions of Cu on Cu(111) and Cu(001): Ab initio evaluation and implications, Phys. Rev. B **73**, 115426 (2006).

[18] C. Busse, W. Langenkamp, C. Polop, A. Petersen, H. Hansen, U. Linke, P. J. Feibelman, and T. Michely, Dimer binding energies on fcc(111) metal surfaces, Surf. Sci. **539**, L560 (2003).

[19] M. Li, P.-W. Chung, E. Cox, C. J. Jenks, P. A. Thiel, and J. W. Evans, Exploration of complex multilayer film growth morphologies: STM analysis and predictive atomistic modeling for Ag on Ag(111), Phys. Rev. B **77**, 033402 (2008).

[20] M. C. Bartelt and J. W. Evans, Dendritic islands in metal-on-metal epitaxy I. Shape transitions and diffusion at island edges, Surf. Sci. **314**, L829 (1994).

[21] J. Zhong, T. Zhang, Z. Zhang, and M. G. Lagally, Island-corner barrier effect in two-dimensional pattern formation at surfaces, Phys. Rev. B **63**, 113403 (2001).

[22] COMSOLMULTIPHYSICS (formerly FEMLAB) is a finite element analysis, solver, and simulation software developed by Comsol, Inc. (www.comsol.com).